A Wavelet Approach for the Identification of Axonal Synaptic Varicosities from Microscope Images

Yu-Ping Wang, *Senior Member, IEEE*, Husain Ragib, and Chi-Ming Huang

***Abstract*—Direct visualization of synapses is a prerequisite to the analysis of the spatial distribution patterns of synaptic systems. Such an analysis is essential to the understanding of synaptic circuitry. In order to facilitate the visualization of individual synapses at the subcellular level from microscope images, we have introduced a wavelet-based approach for the semiautomated recognition of axonal synaptic varicosities. The proposed approach to image analysis employs a family of redundant wavelet representations. They are specifically designed for the recognition of signal peaks, which correspond to the presence of axonal synaptic varicosities. In this paper, the two-dimensional image of an axon together with its synaptic varicosities is first transformed into a one-dimensional (1-D) profile in which the axonal varicosities are represented by peaks in the signal. Next, by decomposing the 1-D profile in the differential wavelet domain, we employ the multiscale point-wise product to distinguish between peaks and noises. The ability to separate the true signals (due to synaptic varicosities) from noise makes possible a reliable and accurate recognition of axonal synaptic varicosities. The proposed algorithms are also designed with a variable threshold that effectively allows variable sensitivities in varicosity detection. The algorithm has been systematically validated using images containing varicosities (≤ 30) that have been consistently identified by seven human observers. The proposed algorithm can give high sensitivity and specificity with appropriate threshold. The results have indicated that the semiautomatic approach is satisfactory for processing a variety of microscopic images of axons under different conditions.**

***Index Terms*—Axonal synapse, granule cell, microscopy, multiscale analysis, neuron image analysis, parallel fiber, peak detection, wavelets.**

I. Introduction

RECENT advances in light microscopy and computer-aided automation have brought about significant improvements in both the quality and quantity of data in image analysis. Improvements in optics such as the use of confocal microscopy have pushed the emphasis of image analysis from the level of cellular architecture to subcellular structural elements. One such structural element is the synapse, the specialized contact zone where one neuron communicates with another. The visualization of synapses, in principle, is the first step leading to the eventual analysis of neuronal circuitry.

Manuscript received October 27, 2005; revised April 14, 2006 and June 20, 2006. This work was supported by NIH AA 13322.

Y.-P. Wang is with the School of Computing and Engineering, University of Missouri-Kansas City, Kansas City, MO 64110 USA (e-mail: wangyup@umkc.edu).

H. Ragib is with TrackIT Solutions, Dubai 500423, United Arab Emirates (e-mail: husain@raghib.com).

C.-M. Huang is with the School of Biological Sciences, University of Missouri-Kansas City, Kansas City, MO 64110 USA (e-mail: huangc@umkc.edu).

Digital Object Identifier 10.1109/TITB.2006.884370

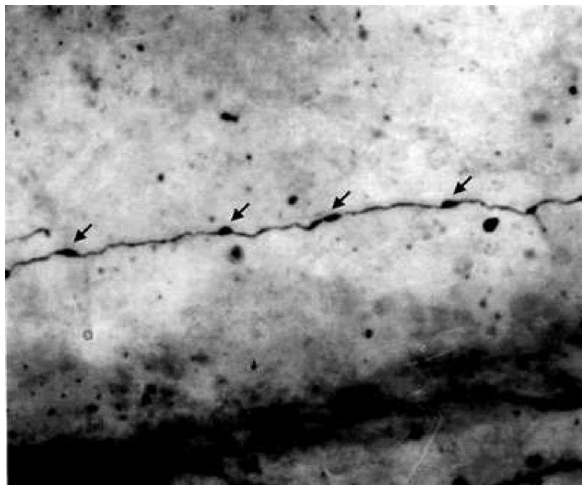

Fig. 1. Microscope image of a parallel fiber taken with oil-immersion objective ($\times 100$). The varicosities are indicated by *arrows*.

At present, the visualization and analysis of synaptic circuity requires serial sections and three-dimensional (3-D) reconstruction from electron microscopy; both are highly labor-intensive endeavors [1]. For example, Shepherd and Harris [1] analyzed 75 axonal segments in the hippocampus for a total of 224 synaptic varicosities over a total length of 674 μm. More recently, they examined synaptic varicosities of 39 granule cell axons reconstructed from 171 electromagnetic (EM) thin sections [3]. In these state-of-the-art studies, no more than a few hundred synapses were identified manually. It would be difficult to introduce a significantly large sample size. If a reliable computer-assisted varicosity identification can be devised, this limit can be further extended, making large-scale analysis of synaptic network feasible.

A near one-to-one correlation, however, has been shown between axonal synapses and their synaptic varicosities, which are visible in light microscopy [2]–[4]. Many investigators have, therefore, drawn inferences at the synaptic level based on light microscope observations of the axonal synaptic varicosities [4]–[6]. However, the large-scale identification and analysis of axonal synaptic varicosities from light microscope observations are still a formidable task. First, typical axonal synaptic varicosities are quite small, some literally at the edge of the optical resolution [4], [6]. Whenever visible, these axonal varicosities are often associated with barely discernable varicosital swellings along the axon fiber (see Fig. 1, for example). The development of an automated, objective, and fast algorithm for the reliable recognition of axonal varicosities from light microscope images of axons is, therefore, a worthy task. Furthermore,

synaptic circuitry of the nervous system is often complex and region-specific. Analysis of the synaptic circuitry must initially be limited to a well-chosen region of the brain. Here, we have chosen the cerebellum for which a great deal of synaptic information is available, and in which promising results are most likely to emerge. More specifically, we have focused on the cerebellar parallel fiber system.

The cerebellar parallel fiber system contains the synapses between the granule cells and the Purkinje cells (gcPc synapses), which have a strategic role in cerebellar function [7], [8]. These synapses link the principal cerebellar cells receiving afferent information, the granule cells, with the principal efferent cells, the Purkinje cells. The selection and timing of the Purkinje cell activation are determined by the density, number, and spacing of these gcPc synapses along the parallel fiber. At the function level, a parallel fiber together with its gcPc synapses can, therefore, be viewed as a message. This message contains the necessary information for the activation of the target Purkinje cells. Hence, the spatial distribution pattern of gcPc synapses along the parallel fibers is of functional significance. All gcPc synapses exhibit long-term depression, widely thought as a physiological substrate of neuroplasticity or learning [9]. A number of other axonal systems, including those in the hippocampus, the corticostriatal fibers, and the cortico-cortical fibers, may function in a similar manner [6].

The present study concerns the analysis of gcPc synaptic varicosities from microscope images of axons (parallel fibers) in an effort to probe the synaptic circuitry of the cerebellar cortex. First, we introduce an algorithm to trace the parallel fibers. There are many image-processing approaches available for tracing the neurites. For example, an automated segmentation algorithm was proposed in [10] that was based on the probability estimation. Guduru *et al*. [11] introduced a modified algorithm of [12], which used a directional derivative filter and seed points. Weaver *et al*. also proposed a heuristic ridge-detection algorithm [13]. In this paper, we used a semiautomatic approach of [14], which offers flexibility in processing complex axons under various imaging conditions. The accurate tracing of axon images facilitates the subsequent identification of varicosities, which is the focus of the paper. Second, we introduce a wavelet-based approach for the recognition of axonal synaptic varicosities along cerebellar parallel fibers. In particular, we employ a special family of differential wavelets designed by one of us [15]. These wavelets are particularly suited to process signals with spiking peaks or discontinuities. This property is ideal for identification of varicosities in microscopy images in that varicosities can be represented as spikes or discontinuities in the data profile of a parallel fiber. We have used these wavelets successfully to enhance the chromosome-banding patterns [16]. Furthermore, these wavelets offer computational advantages [17]. We believe that the development of the automated image analysis technique may hold the key to future efforts in large-scale analysis of synaptic circuitry by directly characterizing the spatial distribution pattern of synapses of an entire synaptic system.

The rest of the paper will be organized as follows. Section II will briefly review the family of differential wavelets. Section III will describe our detection algorithm, which is largely based on the cross-scale correlation properties of varicosities in the wavelet domain. A multiscale point-wise product (MPP) is used to detect significant correlation coefficients relevant to varicosities. Section IV presents the validation of our approach in analyzing real imaging data from microscopy. The paper concludes with discussion on the implication of recognition of synaptic varicosities on the function of the cerebellum in neuroscience studies.

II. Review of Differential Wavelet Representation

A. Redundant Differential Wavelet Representations

Redundant wavelet representations with translation invariance properties are well suited for the detection of signal singularities [17]. In particular, the differential wavelets are a special family of representations ideal for localizing spike patterns in a signal. They are the generalizations of wavelet frames used in [18]. These wavelets are taken as the first-and second-order derivatives of spline functions [15]

$$\psi^n(x) = \frac{d}{dx}\beta^{n+1}(x) \quad \text{or} \quad \psi^n(x) = \frac{d^2}{dx^2}\beta^{n+2}(x) \tag{1}$$

where $\beta^n(x)$ is the B-spline of order n.

The wavelets in (1) approximate the Canny edge detection operator and Laplacian of Gaussian (LoG) filters [17]. Canny and LoG operators have been shown to be optimal for edge detection in a noisy environment. Nevertheless, the advantage of these wavelets is in their ability to provide computational simplicity. If we define the smoothing and wavelet transforms of a signal f at the dyadic scales as $S_{2^j}f$ and $W_{2^j}f$, we can compute the smoothing operation and wavelet transforms using a fast iterative algorithm

$$\begin{cases} S_{2^j}f = S_{2^{j-1}}f * h_{\uparrow 2^{j-1}} \\ W_{2^j}f = S_{2^{j-1}}f * g_{\uparrow 2^{j-1}}, \quad j = 1, 2, \ldots, J \end{cases} \tag{2}$$

where $\{h\}$ and $\{g\}$ are the low-pass and high-pass filters, respectively, and $\uparrow 2^j$ is the up-sampling operation. Through the transform of (2), the signal is decomposed into multiple scales from $1, 2, \ldots, J$. Conversely, the signal can be recovered from its wavelet decompositions

$$S_{2^{j-1}}f = S_{2^j}f * \tilde{h}_{\uparrow 2^{j-1}} + W_{2^j}f * \tilde{g}_{\uparrow 2^{j-1}} \tag{3}$$

where $\{\tilde{h}\}$ and $\{\tilde{g}\}$ are the reconstruction filters. This iterative algorithm is called a pyramid-like algorithm [15], which is similar to the conventional pyramid algorithm [19] except that no downsampling is performed.

The above transform is translation-invariant [15]. This property is ideal for the recognition of peak patterns in multiscale domain. When the signal is decomposed in the multiscale domain, the peak patterns still maintain strong correlations across different resolutions while noncorrelated noise components are mostly left out at higher resolutions. The other advantage is that the filters $\{h\}$ and $\{g\}$ in the wavelet decomposition (2) are binomials and difference operations. Therefore, only additions are needed when they are implemented. Filters of any order can be found in [15]. The following is a list of several filters of lower orders that are used in our experiments.

TABLE I
FIR FILTERS FOR DECOMPOSITION AND RECONSTRUCTION BASED ON THE 0TH-ORDER SPLINES. h AND g ARE THE LOW-PASS AND HIGH-PASS FILTERS USED IN DECOMPOSITION WHILE $\tilde{h}$ AND $\tilde{g}$ ARE THE RECONSTRUCTION FILTERS

taps	h	$\tilde{h}$	g	$\tilde{g}$
-1	$\frac{1}{2}$	$\frac{1}{2}$	-1	$\frac{1}{4}$
0	$\frac{1}{2}$	$\frac{1}{2}$	1	$\frac{1}{4}$

TABLE II
FIR FILTERS FOR DECOMPOSITION AND RECONSTRUCTION BASED ON THE CUBIC SPLINES. h AND g ARE THE LOW-PASS AND HIGH-PASS FILTERS USED IN THE WAVELET DECOMPOSITION WHILE $\tilde{h}$ AND $\tilde{g}$ ARE THE RECONSTRUCTION FILTERS

taps	h	$\tilde{h}$	g	$\tilde{g}$
-4				$\frac{1}{256}$
-3				$\frac{9}{256}$
-2	$\frac{1}{16}$	$\frac{1}{16}$		$\frac{-37}{256}$
-1	$\frac{1}{4}$	$\frac{1}{4}$	-1	$\frac{93}{256}$
0	$\frac{3}{8}$	$\frac{3}{8}$	1	$\frac{-93}{256}$
1	$\frac{1}{4}$	$\frac{1}{4}$		$\frac{-37}{256}$
2	$\frac{1}{16}$	$\frac{1}{16}$		$\frac{-9}{256}$
3				$\frac{-1}{256}$

1) *The Haar-Like Wavelets*: In the extreme case, in which the order of the spline is taken as 0, we obtain the Harr-like wavelets. Table I lists the finite impulse responses (FIRs) of the decomposition and reconstruction filters. These filters (except the normalization constant) are identical to the conventional Haar filters for orthogonal wavelet transforms; the difference between them is that no down-sampling is performed in the decomposition formula (2).
2) *The Cubic Differential Wavelets*: Table II lists the FIRs of cubic differential spline wavelets, which are derived when the order of splines are taken as 1 and 3. These filters have been used in the paper. Different orders of spline filters will result in different denoising effects.

B. Wavelet Approach for Peak Detection

In the next section, we will trace the two-dimensional (2-D) image of a parallel fiber and then project it into a one-dimensional (1-D) signal profile. The synaptic varicosities will correspond to the peak patterns in the 1-D profile. Because of the presence of noise, peak detection is error-prone. This problem can be avoided by detecting the peaks in a multiscale approach. Because the varicosity patterns across several scale resolutions have strong correlations but noises do not, we can enhance the authentic signal while suppressing noises and eliminating incorrect patterns of small size. We have utilized this property for enhancing chromosome-banding patterns [16]. In the Appendix, we model the signals using Gaussian mixtures added with random noise. By analyzing the signal in the multiscale domain, it can be seen that true peak patterns exhibit distinct behaviors from that of the noise. This evidence has also been demonstrated in [16]. Therefore, by comparing these wavelet coefficients at multiple resolutions, the varicosities can be identified more accurately.

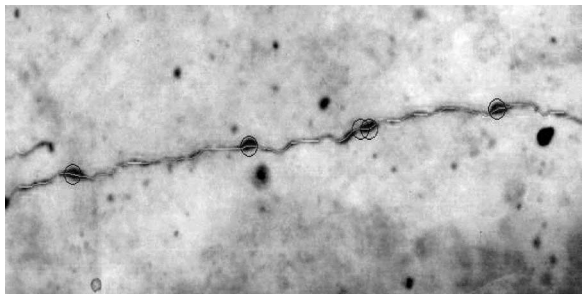

Fig. 2. Varicosities shown in *circles* are detected from the parallel fiber with the proposed algorithm.

III. ALGORITHMS FOR TRACING AND DETECTION OF SYNAPTIC VARICOSITIES

The task of detection of synaptic varicosities is broken down into the following steps.

1) Trace the parallel fibers with varicosities from light microscope images.
2) Generate 1-D profiles of parallel fiber with varicosities by projecting the image intensities along the parallel fiber trace.
3) Locate varicosities in the differential wavelet domains by analyzing the cross-scale correlations of varicosity patterns.
4) Compute quantitative parameters inferred from the locations of varicosities.

Each step is discussed later in detail.

A. Semiautomatic Tracing of Parallel Fibers

The first step is to trace the fiber from the microscope image and record their coordinates with single pixel precision. There are many automated tracing algorithms available [10]–[13]. Because of the complexity of the axonal images under different imaging conditions, we have adopted the semiautomatic tracing algorithm developed in [14] to make certain that the axons are traced efficiently and without error. The other reason for this decision is our consideration that the major focus of the project is the recognition and identification of axonal varicosities. The semiautomatic tracing algorithm offers opportunities for human intervention during the fiber tracing stage.

The code was written in Java and the module was used as a plug-in of NIH Image J. The detection algorithm is based on the eigenvectors of the second derivative matrix computed from the image intensity values. Fig. 2 displays parallel fiber traces using this algorithm. The parallel fiber traces of single pixel width are delineated in the light gray line. The path of the parallel fiber trace is described by a set of coordinates, which will be used in the next step.

B. Projection of Fibers Into 1-D Profiles

Once the parallel fiber of single pixel (medial axis) width is obtained, we project the image along this medial axis within a window. This will convert the fiber into a 1-D profile signal, where high gray-level densities in the profile correspond

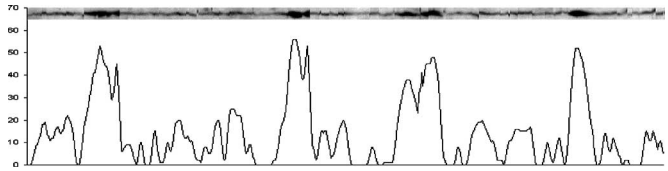

Fig. 3. Parallel fiber in Fig. 2 is straightened and projected into a 1-D data profile within a window of five pixels in which the intensities of the images are inverted in the projection. It can be seen that the peaks in the 1-D profile correspond to the varicosities.

to the synaptic varicosities (indicated by circles in Fig. 2). More specifically, this step is accomplished as follows. We first straighten the parallel fiber trace based on the traced medial axis. The pixels along the normal direction of the medial axis are averaged within a preselected window. In order to make the 1-D projected profile continuous, a linear interpolation is performed to smooth the profile. The height of the vertical window is determined empirically. Fig. 3 shows that the image of the parallel fiber in Fig. 2 is straightened and projected into a 1-D data profile. The image straightening can simplify the computation and has been widely used [20].

The selection of the window size can affect the 1-D profile of fibers and is usually empirically determined based on the data. Selection of an inappropriate window will subsequently result in inaccurate peak detection. If the window size is too big, scattered noise spots may be projected. If the window size is too small, false varicosities might be detected. Fig. 4 shows profile plots (b)–(d) with different window sizes when converting the straightened image (a) to the 1-D profile. Fig. 4(b) shows a more smooth profile than the profiles plotted in (c) and (d) because it uses a larger window. A modest and properly chosen window size can lead to a smooth profile even if the raw optical image may be noisy. We have tested the effect of window size on the peak detection and the height of the window is usually taken to be five pixels. Moreover, the user has an option to specify the window size.

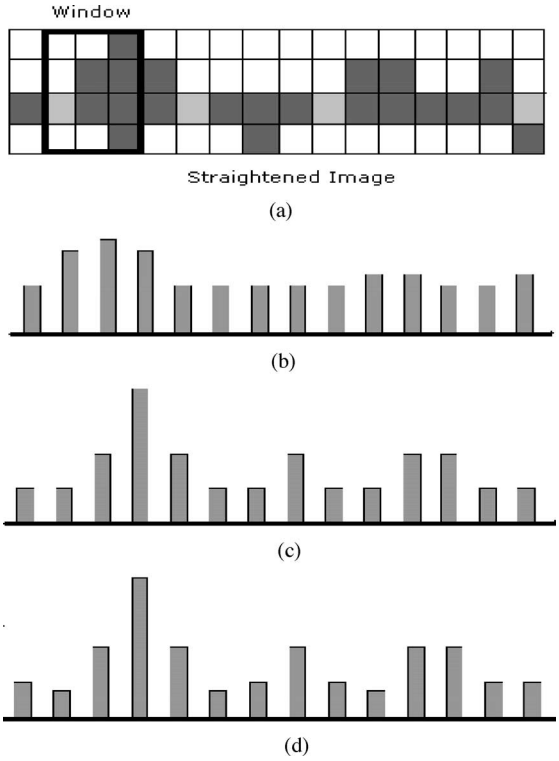

Fig. 4. 1-D data profiles (b–d) are obtained from the projection of 2-D parallel fibers (a) along the medial axis with windows of different sizes, where the height of the window is taken to be three, four, and five pixels, respectively. Varying the size of the window results in slightly different profiles. The optimal window size is determined empirically.

C. Detection of Varicosities in the Wavelet Domain

1) Analysis of Peaks in the Differential Wavelet Domain: The detection of varicosities or peak patterns of the 1-D profile is facilitated by the wavelet transform. If the varicosities are detected directly in the 1-D profile, many small peaks due to noise could be mistakenly located. However, if they are detected in a multiresolution approach, noises will be smoothed out while true peaks can be located more accurately. In the multiscale domain, wavelet coefficients corresponding to true peaks have strong correlations while noises do not. Fig. 5 displays the wavelet decompositions of the 1-D signal profile in Fig. 3 at scales 1–4, as defined in (2). Clearly, with an increase in scale, noises are suppressed while those coefficients corresponding to peaks are maintained. We have analyzed the behavior of white and fractal noises in a separate study [21], which showed that the average number of noise coefficients was reduced to half of that in the previous scale. We can model the varicosities in the 1-D profile as the superimposition of Gaussian functions. They behave differently from noises. A more detailed analysis can be found in the Appendix.

A few approaches exist to detect the peaks, which usually correspond to signal edges or singularities. For example, they can be localized with instantaneous coefficient of variation [22]. In the multiscale domain, an approach that can take an advantage of the correlation of edges between scales is to utilize the MPPs [23]. They are often used in computer vision and image analysis [24], [25]. The MPPs are defined as

$$\mathrm{MPP}_K(n) = \prod_{j=1}^{K} W_{2^j} f(n) \tag{4}$$

where $W_{2^j} f$ is the wavelet decompositions of (2) at scale j. This measurement can exploit the cross-scale correlation due to the presence of desired peaks. Fig. 6 shows the values of the MPPs between two neighboring scales (1–2, 2–3, and 3–4) and the weighted value. It is evident that the MPPs have large values in the vicinity of peaks while they take on smaller values at other locations. We have used MPPs to enhance the banding patterns in a chromosome image [16]. The determination of the first order probability distribution function (PDF) was introduced in [23]. Let $W_{2^i} f$ and $W_{2^j} f$ be the zero-mean joint Gaussian with the covariance matrix

$$C = \begin{pmatrix} \sigma_1^2 & \rho_{12}\sigma_1\sigma_2 \\ \rho_{12}\sigma_1\sigma_2 & \sigma_2^2 \end{pmatrix} \tag{5}$$

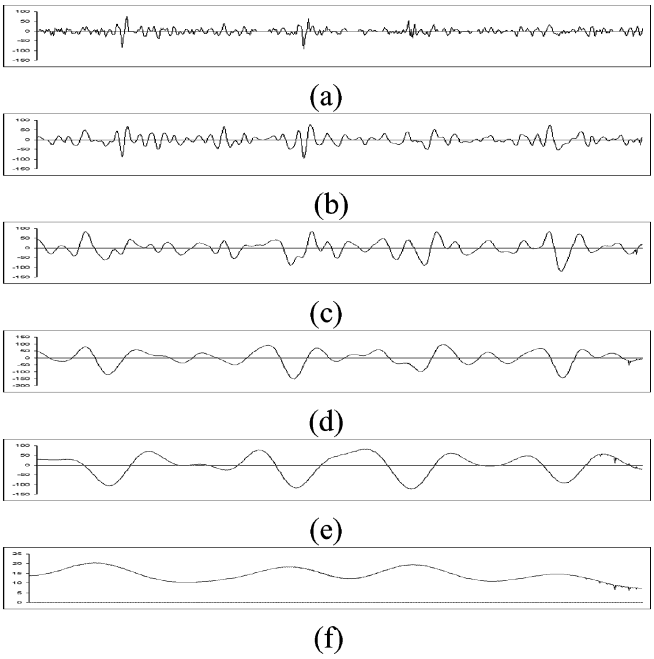

Fig. 5. Differential wavelet decompositions of the 1-D profile in Fig. 3 at scales 1–5. The *bottom panel* is the approximation of the 1-D profile at the coarse scale 5, which smoothes out small noise peaks but maintains strong and salient peaks.

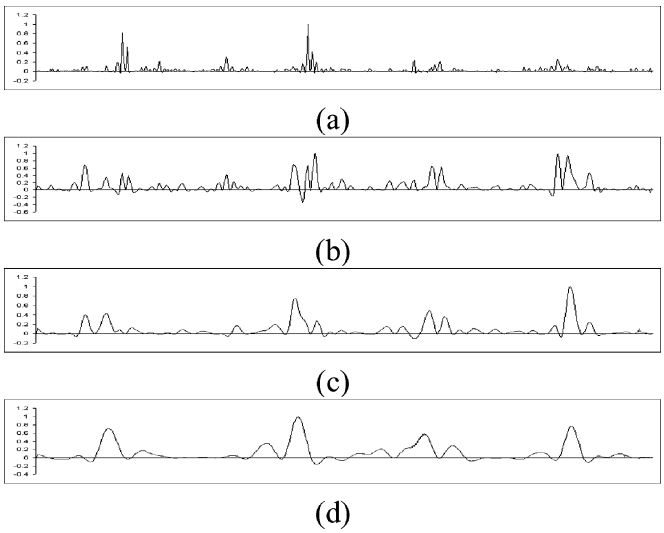

Fig. 6. MPPs between adjacent scales of 1 and 2, 2 and 3, and 3 and 4. The *bottom figure* is the weighted MPPs, which are computed as the weighted combination of MPPs between adjacent scales. The weight of $\{0.2, 0.3, 0.5\}$ is used. The MPPs measure the correlation of the signal patterns between the adjacent scales; they take larger values around the neighborhood of peaks.

where ρ_{12} is the correlation coefficient. Then, the two-scale point-wise product $\text{MPP}_2(K)$ has the PDF

$$\text{PDF}(x) = \frac{1}{\pi\sigma_1\sigma_2\sqrt{1-\rho_{12}^2}}\exp(\rho_{12}\sigma_1\sigma_2 x)K_0(\sigma_1\sigma_2|x|) \quad (6)$$

where K_0 is the modified Bessel function of the second kind and order zero. The PDF of the MPP is generally non-Gaussian [23]. There is a sharp peak when $z = 0$, which indicates that majority of the MPP values are zeros. The larger MPP values have small probability values, which indicates the rare occurrence of the peak patterns. This is consistent with our observation from Fig. 6.

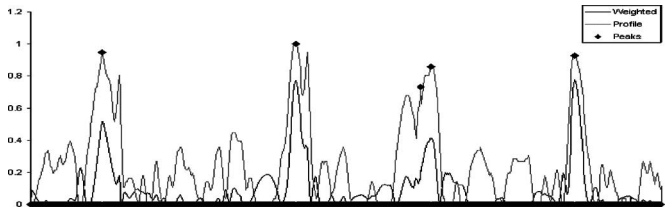

Fig. 7. Detection of varicosities in the 1-D profile by the use of MPPs. The varicosities correspond to the peaks in the profile. The peaks can be accurately localized using coarse-to-fine scale space tracing and the use of the weighed MPPs (*solid line*). The extra peak detected in the original profile can be deleted by using the weighted MPPs. The same weights as in Fig. 6 are used.

D. Detection of Peak Patterns by Making Statistical Decision

Based on the fact that large values of MPP correspond to the occurrence of peaks, we can design the corresponding threshold algorithm to identify the peaks. This can be formulated into a statistical decision problem. We denote the null hypothesis of no peak being present by H_0, and give an upper limit α on the probability of erroneously rejecting H_0 when, in fact, it is true. Then, the decision rule is given by the following: if $\text{MPP}(z) \geq \text{MPP}(\alpha)$, reject the null hypothesis with a confidence of $1-\alpha$; otherwise, do not reject it. In this decision rule, $\text{MPP}(\alpha)$ is the value of the horizontal axis for which the area under the right tail of the PDF is α. The threshold level T is taken as this value, i.e.,

$$\int_T^\infty \text{PDF}(x)\,dx = \alpha. \quad (7)$$

The threshold is actually determined by the confidence level $1-\alpha$. It is critical to choose a proper threshold since an improper threshold may render some noise as peaks, or may skip some varicosities. Equation (7) gives a theoretical guide but is hard to use. In practice, we simply normalize the MPP value to be 0–1 and the threshold is specified in terms of the percentage of the maximum value. Fig. 7 displays the peak determined by a threshold, which can accurately localize the varicosities. Our algorithm is designed with an option to let the users specify different threshold parameters so that different levels of sensitivity can be achieved. This design is useful because real images have different noise levels and the analysis is best carried out with the adjustable levels of sensitivity.

E. Correction of Peak Locations in the Multiscale Domain

The peaks are detected at coarse scale by the analysis of MPP, which reduces the influence of noise. However, due to the inherent uncertainty in time frequency analysis, the locations of these peaks are shifted by smoothing. Therefore, we have to relocate these peaks at the finer scales. The locations of these peaks can be corrected by tracking the detected peaks from a coarser scale to a finer scale. Because of the scaling theorem in

computer vision [17], if there are peaks in the coarse scales, we can always find them in the finer scales. If peaks at coarse scale can be traced at the finer scale within a window, the location of the peak was replaced with that in the coarser scale. The size of the window used for scale-space tracing is also critical. Too small a window could generate false peaks while too large a window could cause true peaks to be missed. The window of size 5 worked well in the experiment. The computation of MPP can be further refined by adjusting the weights of MPP at each scale. Instead of using the MPP at a single scale, we take the weighed average of MPP at several scales. A systematic way of finding optimal MPPs needs further research

$$\overline{\mathrm{MPP}}(n) = \sum_k \omega_k \mathrm{MPP}. \tag{8}$$

At finer scales, there is a high cross correlation while at coarser scales, there is a less cross correlation due to smoothing. Therefore, the weights were chosen such that the MPP at finer scale is given higher weight, and vice versa. This will emphasize the importance of the MPP at finer scales. Fig. 7 demonstrates the improvement brought by this approach.

IV. Validation Experiment

A. Mouse Cerebellum Data Collection

Eight mice (C57BL/6, three months old) were deeply anesthetized and perfused intracardially with 4% formalin and 1% glutaraldehyde. The protocol was executed according to the NIH guidelines, and with the approval of the University of Missouri-Kansas City Institutional Animal Care and Use Committee. The cerebella remained in the partially opened skull and postfixed for 24–48 h before being removed. Each cerebellum was placed in 3% $K_2Cr_2O_7$ and 1% OsO_4 in DH_2O for one day, then washed and impregnated with 1% $AgNO_3$ for one to two days following the rapid Golgi procedure [2]. Coronal sections 75 μm thick were cut for the cerebellum. In optimally stained sections, the Golgi method revealed only a small fraction of randomly selected granule cells, along with their parallel fibers, darkly stained against a pale background. Parallel fiber synaptic varicosities were identified by one of the two protocols. First, we asked experienced human observers to identify varicosities according to guidelines of Palay and Chan-Palay [2] and Pitchipornchai *et al*. [4]. Second, we employed the wavelet-based algorithm for varicosity identification as described in Sections III-A to III-C.

Digital images of parallel fibers were taken using a Zeiss Axiophot light microscope with mountable DCP-11 digital camera. The pictures were taken with $100\times$ oil-immersion objective and stored on the compact flash card that could be transferred to the computer using a compatible converter. A total of 150 varicosities along 22 parallel fiber segments were examined.

B. Validation Experiment

We compared the results from manually identified varicosities by experienced human observers with the wavelet approach. Seven human observers were trained to identify axonal varicosities according to a set of criteria (e.g., the width of the varicosity must be at least 1.5 to 2 times larger than the width of the axon, etc.) [2], [4]. All seven human observers were able to come to perfect agreement on axonal varicosity identification as long as the number of varicosities is relatively small (e.g., $\leq$30). When human observers were assigned to analyze a large number of varicosities (e.g., 3000 per human observer), the standard error of the mean from results of the same observer was between 2.7% and 7.5% in six of the seven human observers while that of one observer was 13.8%. The less-than-perfect agreement among human observers when processing large number of varicosities was a testament of the high level of attention required for varicosity identification and the effect of the fatigue.

In testing our algorithm, we used the images containing varicosities that the human observers were able to identify with consistency. There are several criteria that can be used to quantitatively evaluate the performance of the algorithm. We use the sensitivity metric, a typical criterion that is often used for evaluating the detection performance. Sensitivity by definition is the probability of yielding positive results when a given condition is true. The data set is divided into "true varicosities" and "false varicosities," which denote the presence or absence of the varicosities, respectively. More specifically, a true varicosity is a valid known peak identified by the technician while a false varicosity is not. Tests are then carried out with the wavelet algorithm. The detection results are categorized into positive observations and negative observations. Positive observation is the case that the algorithm correctly identified as the true varicosities while negative observation is the case that the algorithm failed to identify.

Let us consider that there are N_{total} number of varicosities, out of which N_{tp} is the number of true positive observations with varicosities being present. Now let N_{otp} (true positive) be the number of positive observations from N_{tp} positive true observation cases. The sensitivity or true positive fraction (TPF) is defined as the ratio of the number of positive observations to the number of positive true-condition cases [26]

$$\mathrm{TPF} = \frac{N_{\mathrm{otp}}}{N_{\mathrm{tp}}}. \tag{9}$$

We have tested the sensitivity of the algorithm for varicosity recognition. Fig. 8 plots the average sensitivity as a function of different threshold levels, where 10 image data sets have been used. As expected, the sensitivity depends on the threshold. As the threshold value increases, the sensitivity decreases. In the developed software, we give the user an option to select the threshold level so that high sensitivity can be achieved in terms of the degree of the image quality. We have also tested the algorithm under various window sizes. It turns out that the algorithms are quite robust and their performances are not critically dependant on the choice of these parameters.

We also test the sensitivity or true negative fraction (TNF), which is defined as the ratio of the number of negative observations (N_{otn}) to the number of negative true-condition cases (N_{tn})

$$\mathrm{TNF} = \frac{N_{\mathrm{otn}}}{N_{\mathrm{tn}}}. \tag{10}$$

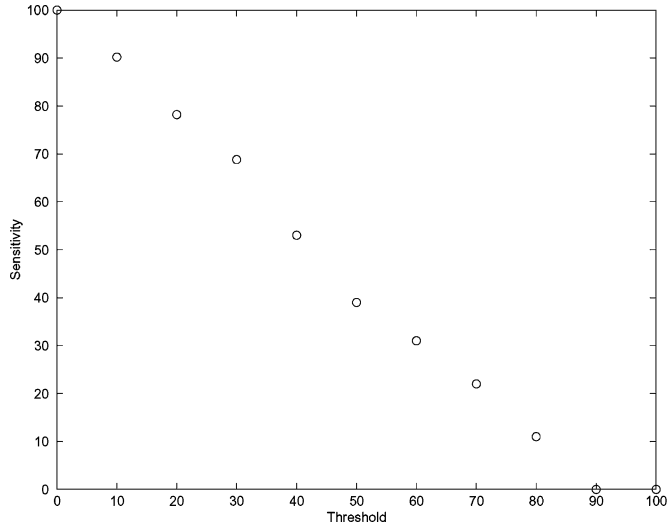

Fig. 8. Plot of the average sensitivity versus the threshold level. The sensitivity decreases with the threshold level. The sensitivity of the test is the probability of its yielding positive results when a given condition is true. A window of five pixels is used in image straightening.

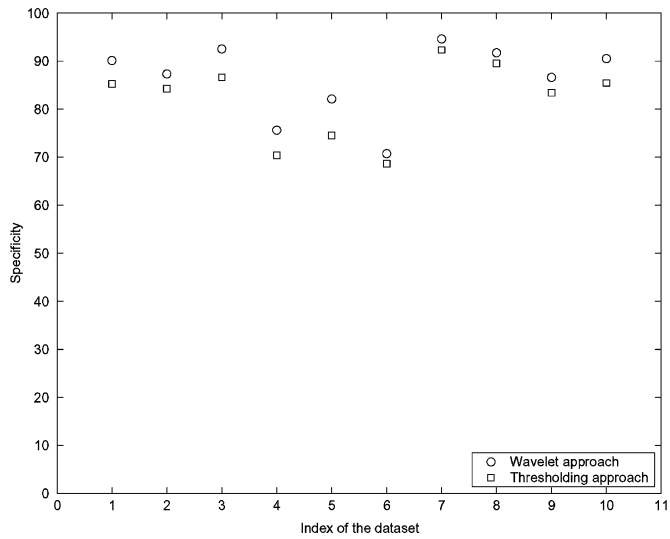

Fig. 9. Comparison of specificity for 10 images between the wavelet-based approach with the simple peak detection within a three-pixel window approach, where the threshold level is taken to be 10.

Fig. 9 shows the specificity of the algorithm when testing on 10 images and the comparison with a conventional algorithm. It demonstrates that the proposed multiscale approach outperforms the conventional thresholding approach, which detects varicosity peak patterns by thresholding within a small window. In addition, the simple thresholding, prone to noise, could falsely identify artifacts as peaks, leading to higher false positive ratios or lower specificity.

We have also used the mean square error (MSE), which is the squared root of the difference between the number of the varicosities detected by the proposed algorithm and the observed ones. MSE decreases with the threshold level (Fig. 10). Thus, at lower threshold levels, we can achieve high sensitivity but some of the nonvaricosities could be falsely detected. For the

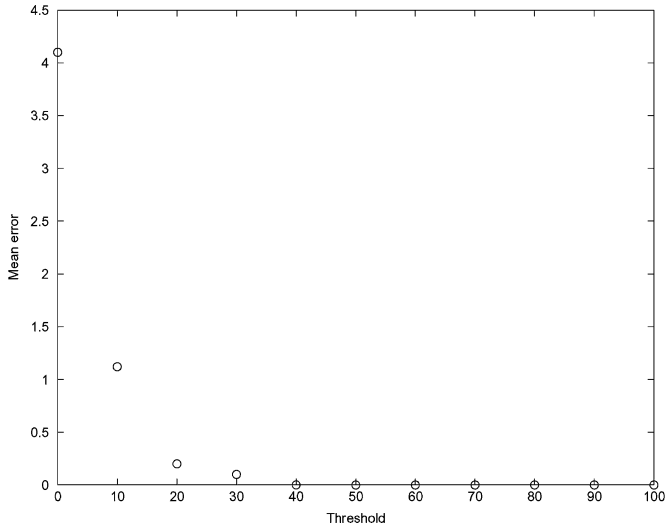

Fig. 10. Plot of MSE, which is defined as the squared root of the difference between the number of the true varicosities and the observed ones.

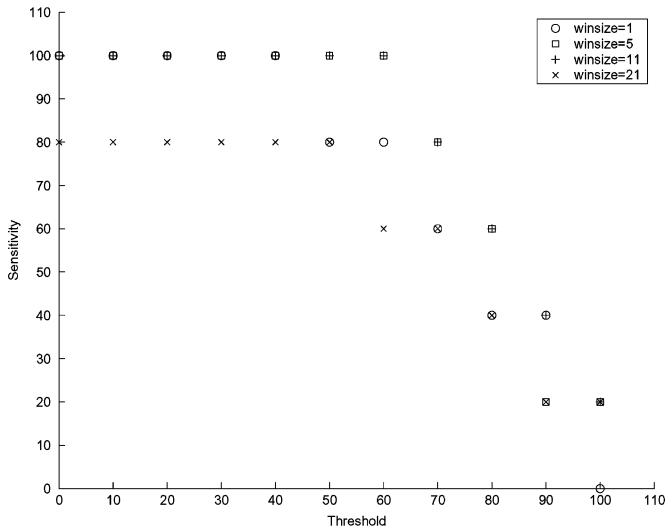

Fig. 11. Test of the effects of different window sizes on the sensitivity when projecting the 2-D image into a 1-D profile (shown in Fig. 3). Within the window size of one to five pixels, the sensitivity of the algorithm remains unchanged.

images that we have tested, our results suggest that a moderate 30% threshold level is the best.

We have also tested the effect of the window size, a parameter used for projecting a parallel fiber to a 1-D profile. The effectiveness of our algorithm is insensitive to window size if the window size is within one to five pixels. As an example, Fig. 11 compares the effects of the window size. It can be seen that the sensitivity of the algorithm remains unchanged within the window size of one to five pixels.

V. Discussion and Conclusion

This paper introduces an automated varicosity-recognition approach using a novel wavelet-based algorithm. We have shown that the identification of synaptic varicosities can be facilitated with wavelet analysis with the proposed differential

wavelets [15]. The facilitation is in the form of automated and reliable detection of peak patterns in the presence of noise. This is because, although it is difficult to separate small varicosities from noise in the spatial domain, they exhibit distinctively different cross-scale correlation when they are transformed into the wavelet domain. The differential wavelets are specially suitable for localizing the spatial correlations because they are translation-invariant representations. In fact, these wavelets perform differential operations by which geometrically important structures, such as varicosities, can be inferred. Furthermore, computational efficiency can be obtained with this family of spline wavelets.

The detection algorithms make use of MPPs to measure the cross-scale correlation of varicosities in the wavelet domain. Considering the varying qualities of images, we have given the user an option to select a threshold in our software. Such a function is useful because it allows the user to conveniently process images with different levels of noise.

Detailed analysis of the synaptic circuitry of a large system in the cerebellum demands detailed knowledge on the spatial distribution pattern of synapses, including axonal synapses of parallel fibers. A key requirement is a high throughput analysis protocol employing a reliable algorithm for the recognition of synaptic varicosities from microscope image of parallel fibers. The wavelet-based method described in this paper should, therefore, represent a significant step in future analysis of the synaptic circuitry. The brain is a complex and dynamic structure. In that sense, the cerebellum is not different from any other sensory, motor, or cognitive center of the brain, except that the cerebellum is involved in all these functions [27]. In principle, the methodology presented here should be generally applicable to such analysis in many other important synaptic systems in neuroscience research. This algorithm helps to reduce the time required for the analysis and the potential errors involved in quantifying the spatial distribution patterns of synapses.

APPENDIX

ANALYSIS OF PEAK PATTERNS IN THE DIFFERENTIAL WAVELET DOMAIN

In the Appendix, we model the varicosities in the parallel fiber as a mixture of Gaussian functions and analyze their behaviors in the wavelet domain.

Suppose that the profile of varicosities along the parallel fiber can be modeled as

$$f(x) = s(x) + n(x) \tag{11}$$

where $s(x)$ is the superimposition of a set of Gaussian functions at different locations

$$s(x) = \sum_{i=1}^{N} c_i G_{\sigma_i}(x, x_i),$$

$$G_{\sigma_i}(x, x_i) = \frac{1}{\sqrt{2\pi}\sigma_i} \exp\left(-\frac{x^2}{2\sigma_i^2}\right) \tag{12}$$

and $n(x)$ is the white noise, with cross correlation

$$E\{n(x)n(x+\tau)\} = \delta(\tau). \tag{13}$$

According to the central limit theorem, the B-splines of order n should approximate the Gaussian function as the order n tends to infinity (even for $n = 3$), i.e.,

$$\beta^n(x) \approx \sqrt{\frac{6}{\pi(n+1)}} \exp\left(-\frac{6x^2}{n+1}\right). \tag{14}$$

They approximate a Gaussian function with the variance $(n+1)/12$. The wavelets defined in (1) are simply the first and second derivatives of B-spline at scale j, which approximate the first and second derivatives of $G_{\sigma_i}(x, 0)$. Thus, the variance of the wavelets at scale j will be approximately $\sigma_j^2 = [(n+1)/12]2^j$. When performing the wavelet transform at scale j, we actually compute

$$W_j s(x) = \sum_{i=1}^{N} c_i G_{\sigma_i}(x, x_i) * \psi_j(x)$$

$$= \sum_{i=1}^{N} c_i G_{\sigma_i}(x, x_i) * \frac{d^p \beta^n(x)}{dx^p} \tag{15}$$

$$\approx \sum_{i=1}^{N} c_i \frac{d^p G_{\tilde{\sigma}_j}(x, x_i)}{dx^p}, \quad p = 1, 2 \tag{16}$$

where we have used the fact that the convolution of two Gaussian functions $G_{\sigma_i}(x, x_i) * G_{\sigma_j}(x, 0)$ is still a Gaussian with a larger variance $\tilde{\sigma}_j = \sigma_i^2 + [(n+1)/12]2^j$. From this formula, we can infer that the locations of the peaks correspond to the local maxima of wavelet of first order or zero crossings of wavelets of second order. This is the mathematical principle behind our analysis algorithm.

For noise, if we take the wavelet transform of (2), it becomes

$$\hat{W}_j n(\omega) = \hat{n}(\omega)\hat{\psi}(2^j\omega) \tag{17}$$

in the spectral domain.

It is easy to have

$$\hat{W}_j n(\omega)\hat{W}_{j+1}\hat{n}(\omega) = \hat{n}^2(\omega)\hat{\psi}(2^j\omega)\hat{\psi}(2^{j+1}\omega). \tag{18}$$

Because $n(x)$ is a white noise, its power spectrum $\hat{n}^2(\omega) = c$, that is, a constant. If we take the inverse Fourier transform, the above-mentioned formula becomes the cross correlation. Following the same procedure for analyzing the $s(x)$, this cross correlation of the wavelet transform of white noise can be approximated by

$$E\{W_j n(x) W_{j+1} n(x+\tau)\} = c\frac{d^p}{dx^p} G_{2j+1}(\tau) \tag{19}$$

when $\tau = 0$; this cross correlation usually becomes zero. This indicates that the cross correlation of the wavelet transforms of noises at two scales is 0. In addition, we have shown that the average number of zero crossings D_j will be decreased to half of the previous one [21]

$$D_j \sim \frac{1}{2^j\sqrt{n+1}}. \tag{20}$$

In other words, if we compute the MPP metrics, about half of them are zeros because half of the zero-crossings or extremes will disappear due to the smoothing operation.

REFERENCES

[1] G. M. G. Shepherd and K. M. Harris, "Three-dimensional structure and composition of ca3 to ca1 axons in rat hippocampal slices: Implications for presynaptic connectivity and compartmentalization," *J. Neurosci.*, vol. 18, pp. 8300–8310, 1998.

[2] S. L. Palay and V. Chan-Palay, *The Cerebellar Cortex: Cytology and Organization*. New York: Springer-Verlag, 1974.

[3] M. A. Friedman, K. M. Harris, and W. G. Regehr, "Three-dimensional comparison of ultrastructural characteristic at depressing and facilitating synapses onto cerebellar purkinje cells," *J. Neurosci.*, vol. 21, pp. 6666–6672, 2001.

[4] C. Pitchipornchai, J. A. Rawson, and S. Rees, "Morphology of parallel fibers in the cerebellar cortex of the rat: An experimental light and electron microscopic study with biocytin," *J. Comp. Neurol.*, vol. 342, pp. 206–220, 1994.

[5] C. Huang, N. Brown, and R. Huang, "Age-related changes in the cerebellum: Parallel fibers," *Brain Res.*, vol. 11, pp. 148–152, 1999.

[6] G. M. G. Shepherd, M. Raastad, and P. Andersen, "General and variable features of varicosity spacing along unmyelinated axons in the hippocampus and cerebellum," *Proc. Nat. Acad. Sci. USA*, vol. 99, pp. 6340–6345, 2002.

[7] D. Marr, "A theory of cerebellar cortex," *J. Physiol.*, vol. 202, pp. 437–470, 1969.

[8] M. Ito, *The Cerebellum and Neural Control*. New York: Raven, 1984.

[9] M. Ito, "Cerebellar long-term depression: Characterization, signal transduction, and functional roles," *Physiol. Rev.*, vol. 81, pp. 1143–1195, 2001.

[10] M. Karim, B. Roysam, N. Dowell, A. Jeromin, M. Yuksel, and S. Kalyanaraman, "Automatic selection of parameters for vessel/neurite segmentation algorithms," *IEEE Trans. Image Process.*, vol. 14, no. 9, pp. 1338–1349, Sep. 2005.

[11] S. K. Guduru, S. V. Narasimhan, S. T. Birchfield, and B. Z. Gao, "Analysis of neurite outgrowth for a laser patterned neuronal culture," presented at the *2nd Int. IEEE EMBS Special Top. Conf. Neural Eng.*, Arlington, VA, Mar. 2005.

[12] A. Can, H. Shen, J. N. Turner, H. L. Tanenbaum, and B. Raysam, "Rapid automated tracing and feature extraction from live high-resolution retinal fundus images using direct exploratory algorithms," *IEEE Trans. Inf. Technol. Biomed.*, vol. 3, no. 2, pp. 125–138, Jun. 1999.

[13] C. Weaver, J. Pinezich, W. Lindquist, and M. E. Vazquez, "An algorithm for neurite outgrowth reconstruction," *J. Neurosci. Methods*, vol. 124, pp. 197–205, 2003.

[14] E. Meijering, M. Jacob, J.-C. F. Sarria, P. Steiner, H. Hirling, and M. Unser, "Design and validation of a tool for neurite tracing and analysis in fluorescence microscopy images," *Cytometry*, vol. 58A, no. 2, pp. 167–176, 2004.

[15] Y.-P. Wang, "Image representations using multiscale differential operators," *IEEE Trans. Image Process.*, vol. 8, no. 12, pp. 1757–1771, Dec. 1999.

[16] Y.-P. Wang, Q. Wu, K. Castleman, and Z. Xiong, "Chromosome image enhancement using multiscale differential operators," *IEEE Trans. Med. Imag.*, vol. 22, no. 5, pp. 685–693, May 2003.

[17] Y.-P. Wang and S. L. Lee, "Scale-space derived from *b*-splines," *IEEE Trans. Pattern Anal. Mach. Intell.*, vol. 20, no. 10, pp. 1050–1065, Oct. 1998.

[18] S. Mallat and S. Zhong, "Characterization of signals from multiscale edges," *IEEE Trans. Pattern Anal. Mach. Intell.*, vol. 14, no. 7, pp. 710–732, Jul. 1992.

[19] I. Daubechies, *Ten Lectures on Wavelets*. Philadelphia, PA: SIAM, 1992.

[20] J. Mohr, A. Hess, M. Scholz, and K. Obermayer, "A method for the automatic segmentation autoradiographic image stacks and spatial normalization of functional cortical activity data," *J. Neurosci. Methods*, vol. 134, pp. 45–58, 2004.

[21] Y.-P. Wang, S. L. Lee, and K. Torachi, "Multiscale curvature-based shape representation using *b*-spline wavelets," *IEEE Trans. Image Process.*, vol. 8, no. 11, pp. 1586–1592, Nov. 1999.

[22] Y. Yu and S. T. Acton, "Edge detection in ultrasound imagery using the instantaneous coefficient of variation," *IEEE Trans. Image Process.*, vol. 13, no. 12, pp. 1640–1655, Dec. 2004.

[23] B. M. Sadler and A. Swami, "Analysis of multiscale products for step detection and estimation," *IEEE Trans. Inf. Theory*, vol. 45, no. 3, pp. 1043–1051, Apr. 1999.

[24] A. Rosenfeld, "A nonlinear edge detection technique," *Proc. IEEE*, vol. 58, no. 5, pp. 814–816, May 1970.

[25] Y. Xu, B. Weaver, D. M. Healy, and J. Lu, "Wavelet domain filters: A spatial selective noise filtration technique," *IEEE Trans. Image Process.*, vol. 3, no. 11, pp. 747–757, Nov. 1994.

[26] A. P. Dhawan, *Medical Image Analysis*. Piscataway, NJ: IEEE Press, 2003.

[27] J. D. Schmahmann, *The Cerebellum and Cognition*. New York: Academic, 1997.

Yu-Ping Wang (M'00–SM'06) received the B.S. degree in applied mathematics from Tianjin University, Tianjin, China, in 1990, and the M.S. and Ph.D. degrees in computational mathematics and communications and electronic systems, respectively, from Xi'an Jiaotong University, Xi'an, China, in 1993 and 1996.

He was a Visiting Fellow at the Center for Wavelets, Approximation and Information Processing of National University of Singapore and Washington University Medical School. From 2000 to 2003, he was a Senior Research Engineer at Perceptive Scientific Instruments, Inc., and then at Advanced Digital Imaging Research, LLC, Houston, TX. In the fall of 2003, he joined the University of Missouri-Kansas City, Kansas City, as an Assistant Professor of computer science and electrical engineering. His current research interests include the interdisciplinary area of bio-imaging, especially at the interface of wavelet research and genetic and genomic imaging.

Husain Ragib received the M.S. degree in interdisciplinary electrical and computing engineering from the University of Missouri-Kansas City, Kansas City, in 2004.

Currently, he is the Lead Software Developer at TrackIT Solutions, Dubai, United Arab Emirates. His current research interests include developing RFID-based application for real-time end-to-end visibility and remote monitoring of critical equipments and assets.

Chi-Ming Huang received the Ph.D. degree in chemistry and biochemistry from the University of California at Los Angeles, Los Angeles, in 1970.

Currently, he is an Associate Professor in the School of Biological Sciences, University of Missouri-Kansas City, Kansas City. Initially, he focused on neurobiology of the cerebellum. His current research interests include developing a method to estimate the length of cerebellar parallel fibers. He has also proposed a model to estimate the coding capacity in cerebellar information processing.